Proceedings of the ASME 2017 International Mechanical Engineering Congress and Exposition
IMECE2017
November 3-9, 2017, Tampa, Florida, USA

IMECE2017-71190

ONE DIMENSIONAL SIMULATION OF DROPLET EJECTION OF DROP-ON-DEMAND INKJET

Huicong Jiang
Mechanical Engineering, Washington State University
Vancouver, WA, USA

Hua Tan
Mechanical Engineering, Washington State University
Vancouver, WA, USA

ABSTRACT

In this study, we present a 1D method to predict the droplet ejection of a drop-on-demand (DoD) inkjet which includes the drop breakup, coalescence, and the meniscus movement at nozzle orifice. A simplified 1D slender-jet analysis based on the lubrication approximation is used to study the drop breakup. In this model, the free-surface (liquid-air interface) is represented by a shape function so that the full Navier-Stokes (NS) equations can be linearized into a set of simple partial differential equations (PDEs) which are solved by method of lines (MOL). The shape-preserving piecewise cubic interpolation and third-order polynomial curve are employed to merge approaching droplets smoothly. The printhead is simplified into a circular tube, and a 2D axisymmetric unsteady Poiseuille flow model is adopted to acquire the relationship between the time-dependent driving pressure and velocity profile of the meniscus. Drop breakup and meniscus movement are coupled together by a threshold of meniscus extension to complete a full simulation of droplet ejection. These algorithms and simulations are carried out using MATLAB code. The result is compared with a high fidelity 2D simulation which was previously developed [10], and good agreement is found. This demonstrates that the proposed method enables rapid parametric analysis of DoD inkjet droplet ejection as a function of nozzle dimensions, driving pressure and fluid properties.

Keywords: DoD inkjet, drop breakup, drop coalescence, meniscus movement, method of lines, unsteady Poiseuille flow

INTRODUCTION

Inkjet printing has advanced significantly since its first commericalisation in 1970s. The dramatic expansion of printing material [1] makes it not only a term decribing graphic printing but also a term covering a range of technologies which involve the ejection of droplets from a printhead onto a substrate. Due to its ability to precisely deliver picoliter-scale volumes of liquid at high speed and low cost, inkjet printing has a wide variety of application in research and manufacturing. These include diverse processes such as additive manufacturing [2], electronic device prototyping [3], pharmaceutics [4], tissue engineering [5] and spray cooling of electronics [6].

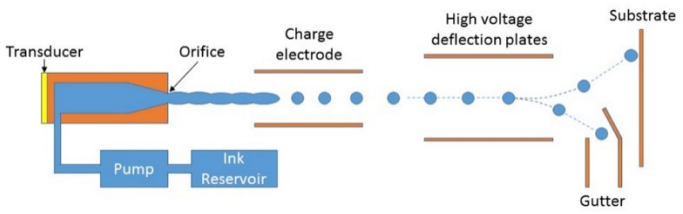

Figure 1. Schematic of CIJ.

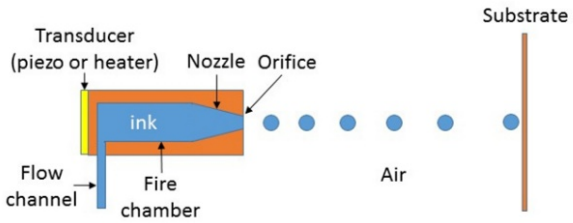

Figure 2. Schematic of DoD inkjet.

Generally speaking, inkjet devices are classified as one of two kinds: countinuous inkjet (CIJ) and DoD inkjet which are distinguished by the form of ejected liquid. The schematic of these two systems are shown in Figure 1-2. The CIJ device ejects a continuous stream of liquid, whereas the DoD device ejects droplets at a regular time interval and is controlled by electronic signals. Further, depending on the actuation of the driving pulse, there are two major varieties of DoD inkjets: piezoelectric inkjet (PIJ) and thermal inkjet (TIJ). For PIJ, the pressure gradient is generated by the deformation of a piezoelectric transducer [7]. In contrast, TIJs use a thin film resistor to boil part of the ink, generating an expanding bubble that pushes ink out of the nozzle [8]. Because the heating element can be microintegrated into the

manufacturing process, TIJ printheads can be packed in a higher density than PIJs which results in a higher printing resolution [9]. The drawback of TIJs is that they are only compatible with certain liquids owing to their heating process.

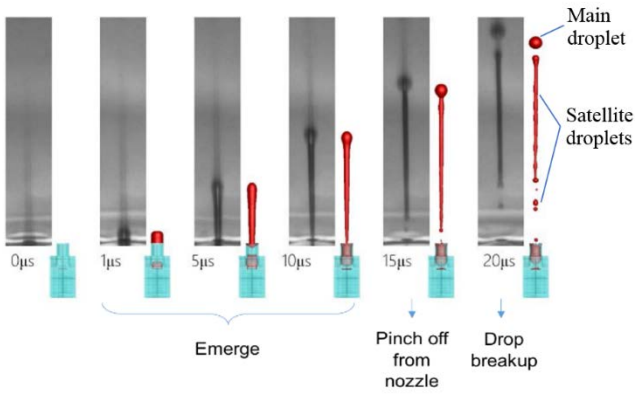

Figure 3. Drop evolution of DoD inkjet : comparision between 3D simulation and experiement.[10]

When the liquid is ejected from the DoD inkjet device, it undergoes a series of physical events: 1. the drop emerges from the nozzle due to actuation; 2. the drop pinches off from the nozzle; 3. the drop breaks up into a main droplet followed by multiple satellite droplets due to Plateau-Rayleigh instablity; 4. the satellite droplets may coalesce or catch up to and recombine with the main droplet. The first 3 events are clearly demonstrated in Figure 3. Satellite droplets often cause a detrimental effect on printing quality, because they tend to scatter on the substrate. Therefore, accurate modelling of breakup and coalescence of droplets is a high priority in the simulation of inkjet droplet ejections.

In the past, we successfully developed a 3D CFD code based on the finite-volume method (FVM) to model the droplet ejection process from inkjet printheads [10]. Although the full-scale CFD simulations can reveal the physical details of droplet ejection (Figure 3), it is not suitable for large scale device design optimization due to high computational costs.

In this paper, to reduce the computational cost, we use a 1D method to model the main process of droplet ejection of DoD inkjets including drop breakup and drop coaelscence as well as meniscus movement at the nozzle orifice, realizing a simulation from driving pressure to drop evolution. Firstly, we use a simplified 1D slender-jet analysis based on the lubrication approximation to study the drop breakup [11]. In this model, the free-surface is represented by a shape function so that the full NS equations can be linearized into a set of simple PDEs of motion which are solved by MOL. Because of the motion of droplets and to circumvent frequent remeshing, the arbitrary Lagrangian-Eulerian method [12] is applied and surface evolution is tracked by a moving uniform staggered mesh in Lagrangian coordinates. Secondly, due to the high sensitivity of shape of droplets and high smoothness requirement in blending area, we use the shape-preserving, piecewise cubic interpolation and third-order polynomial curve to merge approaching droplets smoothly. A minimum distance between droplets is set to avoid wrong merging or late merging. Thirdly, we simplify the printhead into a circular tube and use a 2D axisymmetric unsteady Poiseuille flow model [13] to acquire the relationship between time-dependent driving pressure and the velocity profile of the meniscus. If the meniscus extends to the length of the nozzle orifice radius, the meniscus movement model transitions into the drop breakup model to fully simulate droplet ejection from a DoD inkjet. MATLAB code is used to implement the algorithm and simulation mentioned above.

To ensure that the analytical solution of the velocity profile of the meniscus is correct, we validated it by superposition of starting Poiseuille flow. Under a typical testing driving pressure used by Fromm[14] and Adams [15], the result of the 1D model is compared with a 2D simulation modified from the aforementioned 3D CFD code and good agreement is found. The present research demonstrates that the proposed method enables rapid parametric analysis of droplet ejection from DoD inkjets as a function of nozzle dimensions, driving pressure and fluid properties.

MODEL OF DROP BREAKUP

In this section, we present how to reduce the full NS equations into a 1D problem for an axisymmetric incompressible Newtonian fluid and explain our numerical method.

The droplet ejection process is virtually a liquid-air multiphase flow which involves the solution of the NS equations for both fluids. However, due to the high liquid-air density ratio and extremely short period of droplet ejection time, the viscous force of air can be neglected, i.e. the shear stress along free surface is assumed to be zero. Thus only one phase, the liquid flow, is consider in subsequent analysis.

Given the high velocity of typical inkjet droplets (10-30m/s) and tiny diameter of orifice (10-30μs), the Froude number representing the ratio of inertia force and gravity is very small, and the Bond number representing the ratio of surface tension and gravity is very large, thus we can neglect gravity in the governing equations safely. Supposing dynamic viscosity, surface tension, density and shape function of fluid as μ, σ, ρ and h(z,t), respectively, we have

Navier-Stokes eq.

$$\rho\left(\frac{\partial v_r}{\partial t}+v_r\frac{\partial v_r}{\partial r}+v_z\frac{\partial v_r}{\partial z}\right)=-\frac{\partial p}{\partial r}+\mu\left[\frac{1}{r}\frac{\partial}{\partial r}\left(r\frac{\partial v_r}{\partial r}\right)+\frac{\partial^2 v_r}{\partial z^2}-\frac{u_r}{r^2}\right] \quad (1)$$

$$\rho\left(\frac{\partial v_z}{\partial t}+v_r\frac{\partial v_z}{\partial r}+v_z\frac{\partial v_z}{\partial z}\right)=-\frac{\partial p}{\partial z}+\mu\left[\frac{1}{r}\frac{\partial}{\partial r}\left(r\frac{\partial v_z}{\partial r}\right)+\frac{\partial^2 v_z}{\partial z^2}\right] \quad (2)$$

Continuity eq.

$$\frac{1}{r}\frac{\partial v_r}{\partial r}+\frac{\partial v_z}{\partial z}=0 \quad (3)$$

The non-shear stress assumption gives the first boundary condition (BC):

$$\vec{n}\cdot \mathrm{T}\cdot\vec{t}=0\big|_{r=h} \tag{4}$$

The stress balance in normal direction of interface gives the second BC:

$$\vec{n}\cdot \mathrm{T}\cdot\vec{n}=-\sigma\left(\frac{1}{R_1}+\frac{1}{R_2}\right)\Bigg|_{r=h} \tag{5}$$

In equations (4) and (5), T is the stress tensor in fluid, $\vec{n}$ and $\vec{t}$ are unit vectors normal and tangential to the interface respectively, and R_1 and R_2 are the principal radii of curvature.Obviously, the right-hand side (RHS) of (4) is Young-Laplace equation which represents the capillary pressure difference across the interface. In detail, (4) and (5) are

$$\frac{\mu}{\left(1+h'^2\right)}\left[2h'\left(\frac{\partial v_r}{\partial r}-\frac{\partial v_z}{\partial z}\right)-\left(1-h'^2\right)\left(\frac{\partial v_r}{\partial z}+\frac{\partial v_z}{\partial r}\right)\right]=0\Big|_{r=h} \tag{6}$$

$$\mathrm{p}+\frac{2\mu}{\left(2+h'^2\right)}\left[h'\left(\frac{\partial v_z}{\partial r}+\frac{\partial v_r}{\partial z}\right)-\frac{\partial v_r}{\partial r}-h'^2\frac{\partial v_z}{\partial z}\right]=-\sigma\left(\frac{1}{R_1}+\frac{1}{R_2}\right)\Bigg|_{r=h} \tag{7}$$

$$\frac{1}{R_1}+\frac{1}{R_2}=\frac{1}{h\left(1+h'^2\right)^{1/2}}-\frac{h''}{\left(1+h'^2\right)^{3/2}} \tag{8}$$

where the prime refers to differentiation with respect to z.

Because the radial velocity field at interface is exactly the change rate of shape, it gives the third BC:

$$\frac{Dh}{Dt}=\frac{\partial h}{\partial t}+v_z h'=v_r\big|_{r=h} \tag{9}$$

Note that the object of our model is a slender column of liquid whose axial scale is much larger than the radial scale, thus lubrication approximation can be applied. In this approximation, radial inertia is neglected, and axial velocity and pressure are assumed to be uniform in radial direction, so the Taylor series of v_z and p can be just functions of r:

$$v_z\left(r,z,t\right)=v_0\left(z,t\right)+v_2\left(z,t\right)r^2+\ldots \tag{10}$$

$$p\left(r,z,t\right)=p_0\left(z,t\right)+p_2\left(z,t\right)r^2+\ldots \tag{11}$$

From continuity equation (3) and (10), we obtain

$$v_r\left(r,z,t\right)=-\frac{r}{2}\frac{\partial v_0\left(z,t\right)}{\partial z}-\frac{r^3}{4}\frac{\partial v_2\left(z,t\right)}{\partial z}+\ldots \tag{12}$$

After pluging (10)-(12) into (1), (2) and (6)-(9), and solving these equations to the lowest order in r, we finally transform the NS equations into a 1D problem, i.e. two coupled 1D PDEs of motion:

$$\frac{\partial v}{\partial t}=-v\frac{\partial v}{\partial z}-\frac{\sigma}{\rho}\frac{\partial H}{\partial z}+\frac{3\mu}{\rho h^2}\frac{\partial}{\partial z}\left(h^2\frac{\partial v}{\partial z}\right) \tag{13}$$

$$\frac{\partial h^2}{\partial t}=\frac{\partial}{\partial z}\left(h^2 v\right) \tag{14}$$

$$\mathrm{H}=\frac{1}{h\left(1+h'^2\right)^{1/2}}-\frac{h''}{\left(1+h'^2\right)^{3/2}} \tag{15}$$

in which H is the double of mean curvature which determines capillary pressure.

Previous analysis is all based on Euler coordinates and not compatible with a moving boundary, therefore the equations of motion need to be modified to fit to Lagrangian coordinates. In the pure Lagrangian method, nodes move with the fluid velocity, which often causes severe distortion of mesh after a period of time. As a result, frequent checking of mesh quality and remeshing increases the compuntional cost. To avoid this disadvantage, we use the arbitrary Lagrangian-Euler method to ensure that nodes are always evenly distributed in a droplet.

First, we map a fixed computation space x to the moving physical space *z* [12]:

$$z(x,t)=xL(t)+B(t)\qquad \left(z\in[B,B+L],\ x\in[0,1]\right) \tag{16}$$

where *B* is the z coordinate of the beginning point of liquid, *L* is the length of liquid in physical space. Because of the linear relationship, nodes in physical space always have the same distribution as the computation space.

Now we calculate the total time derivative in computation space with the chain rule. Let's operate on a scalar field $\phi(\mathrm{z},\mathrm{t})$:

$$\frac{d\phi}{dt}=\frac{\partial\phi}{\partial t}+\frac{\partial\phi}{\partial z}\frac{dz}{dt}=\frac{\partial\phi}{\partial t}+\left(x\dot{L}+\dot{B}\right)\frac{\partial\phi}{\partial z} \tag{17}$$

in which $\dot{\mathrm{B}}$ is the the velocity of the beginning node $v_{begin,}$ and $\dot{\mathrm{L}}$ is the contraction/relaxation rate of liquid v_{end}-v_{begin}.

Substituting ϕ with v and h, and inserting them into (13) and (14), we get the modified equations of motion in Lagrangian coordinates. In addition, for completeness, equation (15) is written here again.

$$\frac{dv}{dt}=(x\dot{L}+\dot{B}-v)\frac{\partial v}{\partial z}-\frac{\sigma}{\rho}\frac{\partial H}{\partial z}+\frac{3\mu}{\rho h^2}\frac{\partial}{\partial z}\left(h^2\frac{\partial v}{\partial z}\right) \tag{18}$$

$$\frac{dh^2}{dt}=(x\dot{L}+\dot{B})\frac{\partial h^2}{\partial z}+\frac{\partial}{\partial z}\left(h^2 v\right) \tag{19}$$

$$H = \frac{1}{h\left(1+h'^2\right)^{1/2}} - \frac{h''}{\left(1+h'^2\right)^{3/2}} \quad (20)$$

We reiterate that the velocity and height are not tracked by the pure Lagrangian coordinates and the nodes do not move with fluid streamlines. This Lagrangian coordinates is defined by equation (16), and that is why (18) and (19) still retain the advection term.

Discrete equations of motion (18)-(20) are solved by MOL [16] subject to appropriate BCs and initial conditions (ICs). Specifically, we define a uniform staggered mesh in computational space and use the finite difference method to represent all the partial spatial derivative term in RHS of (18)-(20). For example, we apply a first order upwind scheme for the advection term and second order central difference scheme for the other terms. In this way, (18) and (19) are transformed into two ordinary equations with only the partial time derivative of v and h on the left-hand side (LHS). We integrate v in one set of nodes and integrate h and H in the other set of staggered nodes as shown in Figure 4. Ultimately the MATLAB ODE solver routine 'ode23t' is used to implement MOL.

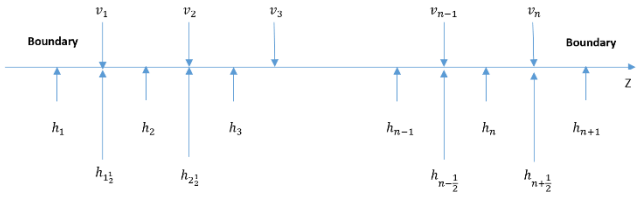

Figure 4. Uniform staggered mesh.

MODEL OF DROP COALESCENCE

The first thing we need to figure out in drop coalescence is how to judge when a coalescence is going to happen. To avoid an immediate coalescence after breakup and overlap caused by late coalescence, we give the following condition:

$$(v_2 - v_1) \times dt > 0.8\Delta L \quad (21)$$

in which v_1, v_2, dt and ΔL are velocity of the tail node of the first droplet, velocity of the head node of the second droplet, time step and distance between two droplets respectively which are shown in Figure 5(a). If this condition is satisfied, a coalescence happens.

Note that although mesh is evenly distributed in a droplet all the time, different droplets usually have different mesh intervals due to extension and contraction. Accordingly, before blending, we need to remesh the whole space occupied by the merged droplet with a uniform mesh. This procedure is shown in Figure 5(b). Because the evolution of drop is highly sensitive to its shape, we choose the shape-preserving piecewise cubic interpolation to evaluate the height and velocity at remeshed nodes.

After remeshing, two nodes nearest to the approaching ends can be identified which is shown in Figure 5(c). We call these two nodes clip points because the area between them, namely blending area, will be clipped out for shape reconstruction.

Hanchak [12] found that the smoothness of the blending area is paramount for numerical stability, therefore we follow the third-order polynomial curve to construct a smooth contour in the blending area which means, except for the clip point, at least two more equations are needed to determine the curve. These two equations are given by a throat which is located in the center of blending area with a height of 1% of orifice radius and a slope of zero. Figure 5(d) shows the result of drop coalescence with a highlight on blending area and throat.

While this blending method is reliable and robust, it does add a small amount of mass into the system. We examined several instances and found that the additional mass is less than 1% of the whole drop and is therefore negligible.

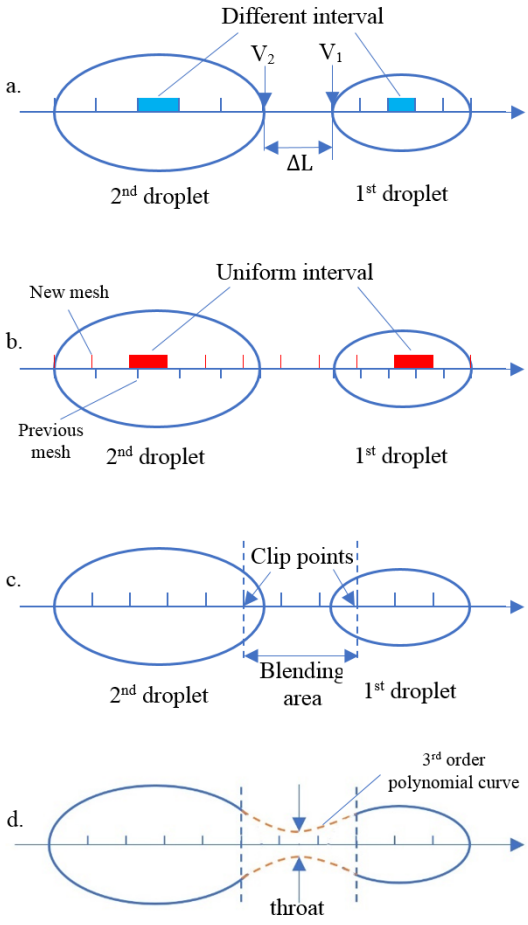

Figure 5. Numerical procedure of drop coalescence: a) two approaching droplets with different mesh interval. b) remeshing the whole space occupied by the merged droplet with a uniform mesh. c) finding clip points and blending area. d) a merged droplet after reconstruction of the blending area.

MODEL OF MENISCUS MOVEMENT

The structure of DoD inkjet printhead is diverse and complicated. For example, the PIJ has four kinds of mode: squeeze, bend, push and shear [17], and all of them have different structures. In general, a DoD inkjet printhead consists of three main components: firing chamber, ink flow channel and nozzle. However, for simplicity and to lower the computational burden, we just consider the printhead as a circular tube so that a 2D axisymmetric unsteady Poiseuille flow model can be applied to mimic the movement of meniscus.

In this section, we start from the governing equations for Poiseuille flow to derive an analytical solution of velocity profile and demonstrate the way to couple the meniscus model with the drop breakup model.

In Poiseuille flow, only the axial velocity component is considered, which means that the NS equations is reduced into

$$\rho\frac{\partial u}{\partial t}=-\frac{\partial p}{\partial z}+\frac{\mu}{r}\left(\frac{\partial u}{\partial r}+r\frac{\partial^2 u}{\partial r^2}\right) \tag{22}$$

With the following scalar (23), (22) can be transformed into dimensionless form (24):

$$u^*=\frac{u\mu L}{r_0^{\,2}\Delta p}\quad t^*=\frac{tL}{r_0^{\,2}\rho}\quad r^*=\frac{r}{r_0}\quad p^*=\frac{p}{\Delta p}\quad z^*=\frac{z}{L} \tag{23}$$

$$\frac{\partial u^*(t^*,r^*)}{\partial t^*}=-p_z{}^*(t^*)+\frac{1}{r^*}\frac{\partial u^*(t^*,r^*)}{\partial r^*}+\frac{\partial^2 u^*(t^*,r^*)}{\partial r^{*2}} \tag{24}$$

in which r_0 is the radius of orifice and L is the length of nozzle.

By performing a Laplace transform for (24) with respect to t^* and applying initial condition $u^*(0,r^*)=0$, we get an ODE:

$$\frac{d^2\bar{u}}{dr^{*2}}+\frac{1}{r^*}\frac{d\bar{u}}{dr^*}-s\bar{u}=\bar{p}_z \tag{25}$$

in which $\bar{u}$ is a function of s and r^*, while $\bar{p}_z$ depends on s only.

A particular solution of (25) is $\bar{u}=-\bar{p}_z/s$ and the corresponding homogeneous equation can be written as Bessel's differential equation with assumption $\eta=ir^*\sqrt{s}$:

$$\eta^2\frac{d^2\bar{u}}{d\eta^2}+\eta\frac{d\bar{u}}{d\eta}-\eta^2\bar{u}=0 \tag{26}$$

Therefore, the general solution of (26) is

$$\bar{u}=c_1J_0(ir^*\sqrt{s})+c_2Y_0(ir^*\sqrt{s})-\frac{\bar{p}_z}{s} \tag{27}$$

Through BCs of $\bar{u}(s,0)=finite$ and $\bar{u}(s,1)=0$, the c_2 is determined as zero and $\bar{u}$ is simplified as

$$\bar{u}=\frac{\bar{p}_z}{s}\left[\frac{J_0(ir^*\sqrt{s})}{J_0(i\sqrt{s})}-1\right]=\bar{p}_z\bar{g} \tag{28}$$

From the residue thorem for contour integrals, the inverse Laplace transform of $\bar{g}$ is

$$g(t^*)=\frac{1}{2\pi i}\int_{\gamma+i\infty}^{\gamma+i\infty}\bar{g}e^{st^*}ds=\sum\mathrm{Res}\left[\bar{g}e^{st^*}\right]=\sum_{n=1}^{\infty}\frac{2J_0(-b_nr^*)}{b_nJ_1(-b_n)}e^{-b_n^{\,2}t^*} \tag{29}$$

where γ is an arbitrary real number that is sufficiently positive and b_n is the eigen value of $J_0(i\sqrt{s})=J_0(b_n)=0$.

With the convolution theorem, the dimensionless analytical solution for u^* driven by time-dependent pressure gradient $p_z{}^*(t^*)$ is

$$\begin{aligned}u^*(t^*,r^*)&=\int_0^{t^*}p_x(\tilde{t})g(t^*-\tilde{t})d\tilde{t}\\&=\sum_{n=1}^{\infty}\frac{2J_0(b_nr^*)}{b_nJ_1(-b_n)}\int_0^{t^*}p_z{}^*(\tilde{t})e^{b_n^{\,2}(\tilde{t}-t^*)}d\tilde{t}\end{aligned} \tag{30}$$

where

$$p_z{}^*(t)=\frac{P_{orifice}(t)-P_{drive}(t)}{\Delta p} \tag{31}$$

Obviously, the only unkown in (30)-(31) is $P_{orifice}$. Since $P_{orifice}$ is capillary prsessure which is determined by the shape of meniscus , we can always derive the initial velocity of meniscus from an initial shape. Then the initial velocity can yield the the shape of next time step which will further produce the velocity of next time step. As this loop continues, we can acquire the shape and velocity of meniscus at any moment.

Although the accurate shape of meniscus demands many points to depict, we just use a segment of sphere determined by the position of vertex to represent it, which is shown in Figure 6(b). This simplification can greatly ease the calculation, because we only need to consider the centerline velocity $u^*(t^*,0)$ (32) and have an analytical solution of $P_{orifice}$ (33)-(34).

$$u^*{}_{center}=u^*(0,t^*)=\sum_{n=1}^{\infty}\frac{-2}{b_nJ_1(b_n)}\int_0^{t^*}p_z{}^*(\tilde{t})e^{b_n^{\,2}(\tilde{t}-t^*)}d\tilde{t} \tag{32}$$

$$R_N=R_T=\frac{a^2+r_0^{\,2}}{r_0}\qquad(-r_0\le a<r_0) \tag{33}$$

$$P_{orifice}=\sigma\left(\frac{1}{R_N}+\frac{1}{R_T}\right) \tag{34}$$

The R_N and R_T and a in (33) are normal and tangential principle radus of meniscus, and extension of vertex. Equation (34) is the Young-Laplace equation.

Nevertheless a segment of sphere is unable to represent the meniscus, if the extension of vertex is less than negative orifice radius, such as the case in Figure 6(a). Actually this scenario happens a lot, especially at the start of a pressure wave where a strong negative pressure suck the meniscus into nozzle. In this case, we switch to an hemi-ellipsoid to represent the meniscus. The expression of R_N and R_T are given in (35).

$$R_N = r_0 \qquad R_T = \frac{r_0^2}{a} \qquad (a < -r_0) \tag{35}$$

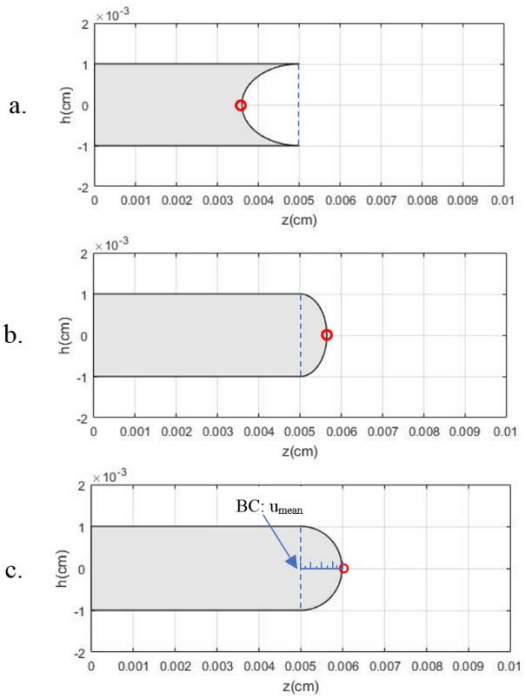

Figure 6. Different stage of meniscus: a) hemi-ellipsoid: the extension of vertex is less than negative orifice radius due to negative driving pressure at the start of a pulse. b) segment of sphere: the extension of vertex is shorter than orifice radius c) first coupling moment: the extension of vertex reaches positive orifice radius and the hemisphere is discretized by a uniform staggered mesh. The boundary condition of drop breakup model is the mean velocity at nozzle orifice. The blue dash line is the position of orifice and the red circle is the position of vertex

The meniscus can not extend without limitation. When the extension of the vertex is larger than the orifice radius, i.e. the shape of meniscus reaches a positive hemisphere, the model of drop breakup starts to couple. The initial condition is provided by the discretization of hemisphere with a uniform staggered mesh and the assumption that the hemisphere moves uniformly with the mean velocity. The boundary condition is determined by the mean velocity at orifice all the time. In (35) we find that the mean velocity is also a function of $p_z^*(t^*)$, thus according to (31) (33) and (34), the boundary condition can definitely couple with the drop breakup model which updates the shape of droplet.

$$u^*_{mean} = \frac{1}{\pi}\int_0^1 u \cdot 2\pi r^* dr^* = \sum_{n=1}^{\infty} \frac{-4}{b_n^2} \int_0^{t^*} p_z^*(\tilde{t}) e^{b_n^2(\tilde{t}-t^*)} d\tilde{t} \tag{35}$$

Specifically, after a time step, the drop breakup model outputs a new shape of drop and the velocity along it. By applying (20) and (34), this new shape produces a new $P_{orifice}$ which can be subsituted into (35) to yield a new mean velocity. This new mean velocity again becomes the new boundary condition. By the loop, the two models are coupled together.

Up to now, we only used u_{mean} and u_{center} in the model of meniscus, although the analysis of velocity profile is based on 2D. Hence our simulation is still a 1D problem.

RESULT

The mean velocity at orifice is the most critical factor in our 1D method, because it is the joint between drop breakup model and meniscus model. To ensure the correctness of the complex equation of u_{mean} (23), which is also an indirect validation of (30), we compared it with the superposition of starting Poiseuille flow (35). Referring to [18] and [19], one can find the detailed derivation of (35).

$$\frac{u(t,r)}{u_{max}} = \left[1-\left(\frac{r}{r_0}\right)^2\right] - \sum_{n=1}^{\infty} \frac{8J_0(b_n r/r_0)}{b_n^3 J_1(b_n)} \exp\left(-b_n^2 \frac{\nu t}{r_0^2}\right) \tag{35}$$

where

$$u_{max} = \frac{-p_z r_0^2}{4\mu} \tag{36}$$

As can be seen in (35), the summation is a damping function. When t=0, u is minimum 0 and the summation is maximum $1-(r/r_0)^2$, and when t goes to inifinity, u reaches its maximum $[1-(r/r_0)^2]u_{max}$ (fully developed flow) and the summation reaches minimum 0. Therefore, during the damping period (from the second time step), for every component u in superposition which reach its maximum u(dt) at first time step, the summation should multiply a factor λ to make it reach u(dt) when t=dt.

$$\lambda(r) = \frac{u(dt,r)}{u_{max}\left[1-(r/r_0)^2\right]} \tag{37}$$

As a consequence, the expression of superposition is

$$u(t_i,r) = u^i(dt,r) + \sum_{k=1}^{i-1}\left[\lambda^k(r) u^k_{max} \sum_{n=1}^{\infty} \frac{8J_0(b_n r/r_0)}{b_n^3 J_1(b_n)} \exp\left(-b_n^2 \frac{\nu t_{k-1}}{r_0^2}\right)\right] \tag{38}$$

where the superscript represents the time step.

By comparison in Figure 7, we can find the dash line (solution of superposition) almost overlaps the blue solid line (analytical solution) and both of them has a short time lag behind

the purple solid line which is the driving pressure wave. This confirms that the analytical solution of the mean velocity at the orifice is correct.

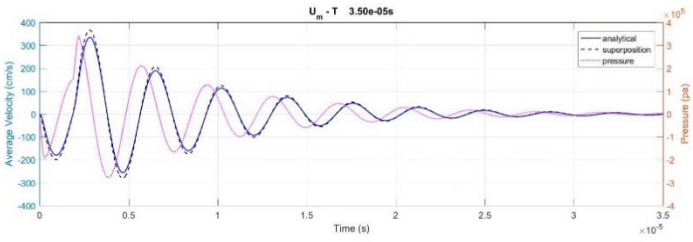

Figure 7. Comparison of different solutions of mean velocity at the orifice: the blue solid line is the analytical solution, and the dashed line is the solution of superposition. The purple solid line is the driving pressure wave.

To validate the whole 1D method by using the following ink properties and nozzle dimensions (39), we compare our result with a high fidelity 2D simulation modified from the previously developed 3D CFD code [8] under a typical testing driving pressure (Table 1 and Figure 8) used by Fromm [14] and Adams [15].

$$\rho = 1.135\text{g/cm}^3 \quad \sigma = 67.26\text{dym/cm} \quad \mu = 0.0615\text{P}$$
$$r_0 = 10\mu\text{m} \quad L = 50\mu\text{m} \tag{39}$$

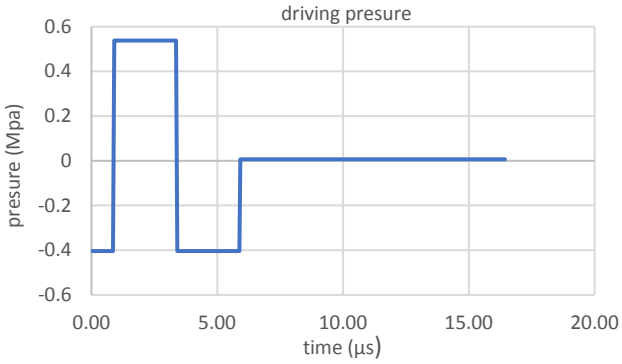

Figure 8. A typical testing driving pressure.

$t/\left(r_0\sqrt{\frac{\rho r_0}{\sigma}}\right)$	$P/\left(\frac{r_0}{\sigma}\right)$
0.00 - 0.21	-60
0.21 - 0.82	+80
0.82 - 1.43	+60
1.43 -	+1

Table 1. A typical testing driving pressure.

As shown in Figure 8, the 1D and 2D method agree closely in the first 5μs where includes the meniscus movement and models coupling. This indicates good performance of our simplification in the meniscus model. After 7μs (Figure 9), a significant difference appears. The meniscus of the 2D method has an overturned surface around the orifice which is unable to be described by the shape function of 1D method, but the shape out of the orifice is still in good agreement. Besides, it is noteworthy that the first breakup of both methods are slightly after 11μs, which demonstrates a good temporal accuracy of the 1D method. At 20μs (Figure 10), the relative speed of both drops changes. Due to its longer tail and larger mass, the drop modeled by the 2D method is passed by that of the 1D method and the distance between them keeps increasing after 28μs where both drops are in uniform motion with different velocities.

Figure 11 shows the comparison of drop volume where the 1D and 2D method has a final volume of 4.06pl and 4.56pl respectively. The 11% difference is quite acceptable, considering the inevitable mass loss caused by overturned surface in 1D method. Comparison of average velocity which is the quotient of the total momentum and total mass is shown in Figure 12. The 1D method becomes stable in 538cm/s, and the 3D method has a final average velocity of 492cm/s. Under the same driving pressure, the reduced mass of the 1D method results in its higher velocity.

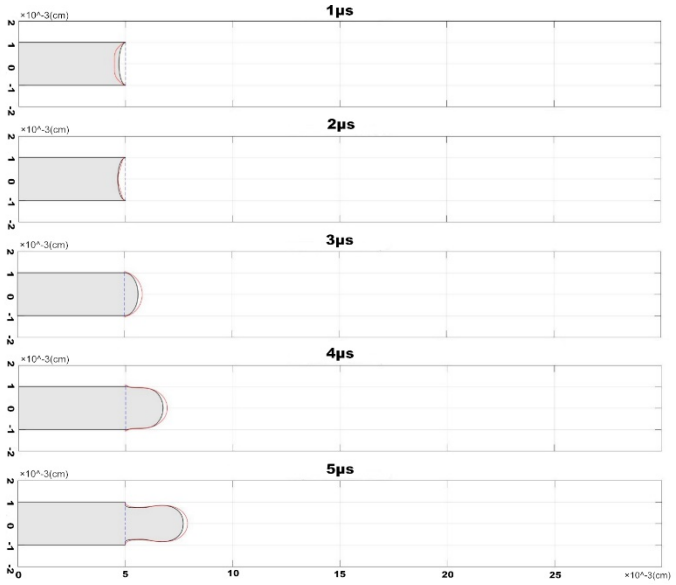

Figure 8. Meniscus movement and drop evolution in 1-5μs: the red solid line is the result of 2D simulation and the filled area is the drop of 1D method.

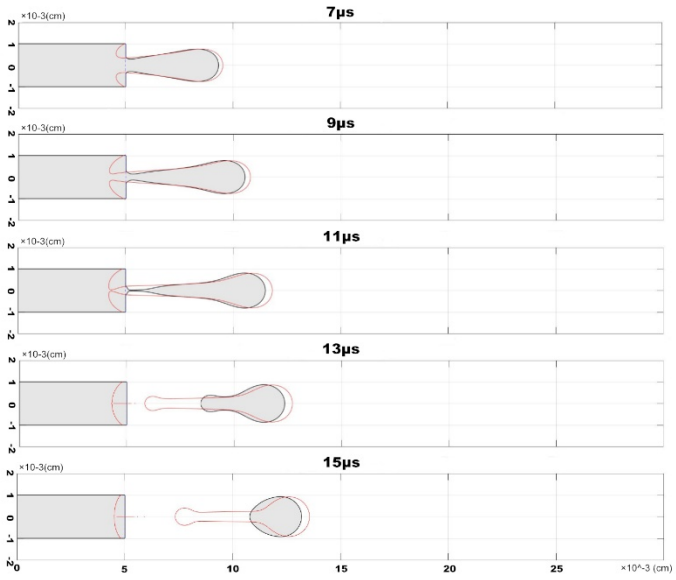

Figure 9. Drop evolution in 7-15μs: The breakup time of 1D and 3D method are very close which is slightly behind 11 μs.

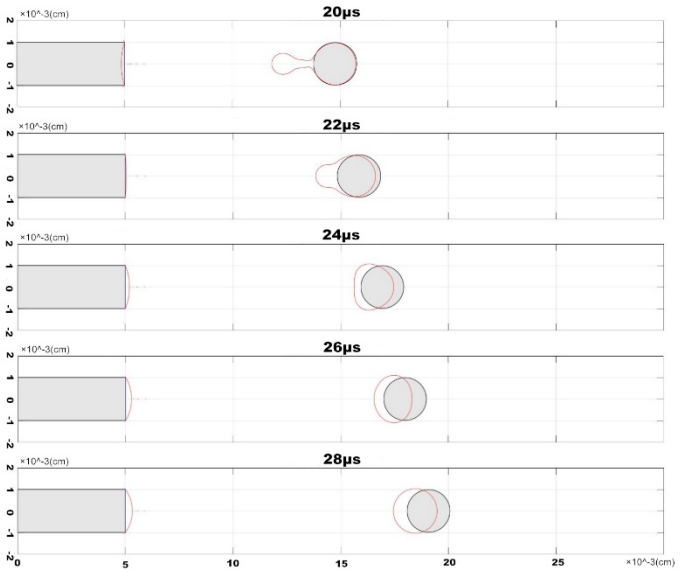

Figure 10. Drop evolution in 20-28μs: the drop of the 1D method surpasses the 2D method.

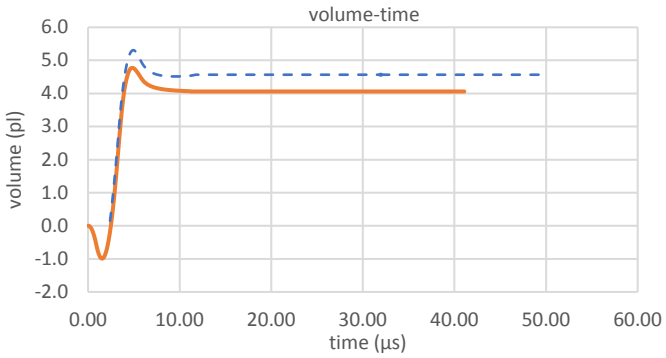

Figure 11. Comparison of drop volume: the solid line represents the 1D method and the dash line represents the 2D method.

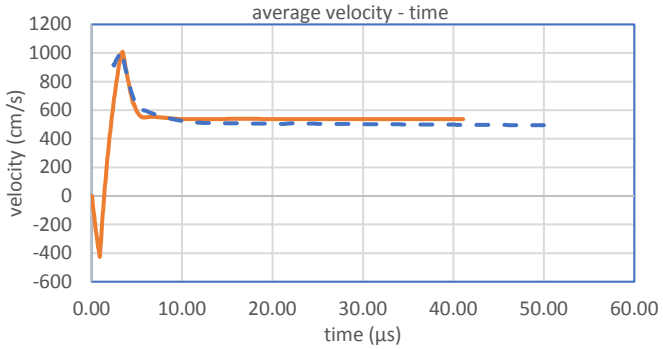

Figure 12. Comparison of mean velocity: solid line represents the 1D method and dash line represents the 2D method.

From Figure 3 and Figure 8-11, we can find that the drop is a slender filament when it first pinches off from the nozzle. This kind of shape matches the lubrication analysis in drop breakup model very well. However, after a period of time, the contraction will definitely make the drop not slender anymore, and eventually the drop will become an oscillating sphere. Can the drop breakup model describe the contraction and oscillation accurately? To look at it more closely, we compare the horizontal length of drop in 1D and 2D methods by a stationary filament (Figure 13). Properties of liquid and dimensions of filament are

$$\rho = 1\text{g/cm}^3 \quad \sigma = 1\text{dym/cm} \quad \mu = 0.45\text{P} \quad r_0 = 0.2\text{cm} \quad L = 1.8\mu\text{m} \qquad (40)$$

Thus the ohnesorge number is 0.1 and the ratio of length and radius is 9 which are reasonable parameters for ink filament and, more importantly, can guarantee an evolution of contraction and oscillation without breakup [20].

In Figure 13, good agreement is found before the drop reaches its minimum horizontal length where is exactly the period of contraction. After that, the oscillation amplitude and frequency of two methods diverge a lot. The intrinsic higher dissipation of 1D method during oscillation period results in the

its faster damping. Fortunately, compared with the contraction, oscillation does not substantially affect the droplets movement and evolution.

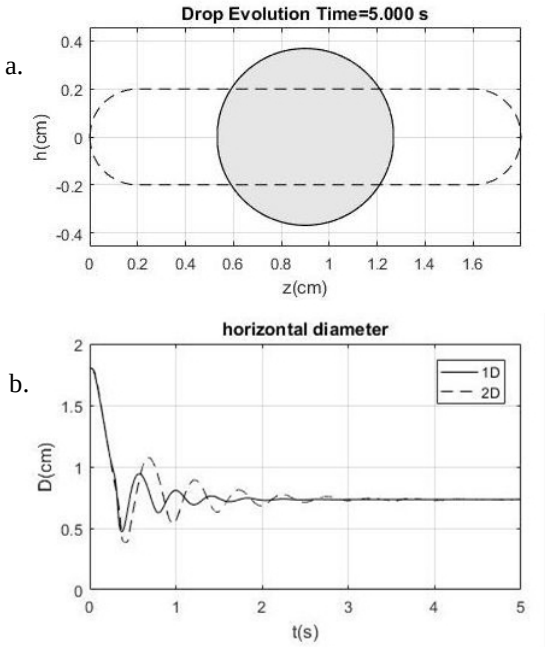

Figure 13. Comparison of filament contraction and oscillation: a) filament shape: the dash line is the initial shape and the filled area is the shape at the fifth second. B) horizontal length: the solid line represents the 1D method and the dash line represents the 2D method.

CONCLUSION

We proposed a 1D numerical method to predict the droplet ejection of DoD inkjets including the drop breakup, drop coalescence and movement of meniscus. The model of drop breakup is based on lubrication approximation and solved by MOL in a moving mesh. The model of drop coalescence reconstructs the blending area between approaching droplets, realizing a smooth and stable merge. The model of meniscus movement bridge pressure and velocity profile through the unsteady Poiseuille flow. The overall 1D method is validated by a comparison with a high fidelity 2D simulation we developed before and good agreement is achieved. This work demonstrates that the proposed method enables rapid parametric analysis of droplet ejection of DoD inkjet as a function of nozzle dimensions, driving pressure and fluid properties.

Acknowledgements

We would like to thank the Office of Research Support & Operations of Washington State University (WSU) for their support through the New Faculty Seed Grant Program (#128044-001). We also would like to thank the Office of Academic Affairs of WSU-Vancouver for additional financial support. The first author would like to thank Brett Merritt for proofreading the manuscript.

REFERENCES

[1] Calvert, Paul. "Inkjet printing for materials and devices." *Chemistry of materials* 13.10 (2001): 3299-3305.

[2] Thomas, Helen R., Neil Hopkinson, and Poonjolai Erasenthiran. "High speed sintering—continuing research into a new rapid manufacturing process." *Proceedings of 17th SFF Symposium, Austin, TX*. 2006.

[3] Kawahara, Yoshihiro, et al. "Instant inkjet circuits: lab-based inkjet printing to support rapid prototyping of UbiComp devices." *Proceedings of the 2013 ACM international joint conference on Pervasive and ubiquitous computing*. ACM, 2013.

[4] Daly, Ronan, et al. "Inkjet printing for pharmaceutics–a review of research and manufacturing." *International journal of pharmaceutics* 494.2 (2015): 554-567.

[5] Saunders, Rachel Elizabeth, and Brian Derby. "Inkjet printing biomaterials for tissue engineering: bioprinting." *International Materials Reviews* 59.8 (2014): 430-448.

[6] Bash, Cullen E., Chandrakant D. Patel, and Ratnesh K. Sharma. "Inkjet assisted spray cooling of electronics." *ASME 2003 International Electronic Packaging Technical Conference and Exhibition*. American Society of Mechanical Engineers, 2003.

[7] Wijshoff, Herman. "The dynamics of the piezo inkjet printhead operation." *Physics reports* 491.4 (2010): 77-177.

[8] Tan, Hua, et al. "Numerical simulation of droplet ejection of thermal inkjet printheads." *International Journal for Numerical Methods in Fluids* 77.9 (2015): 544-570.

[9] Castrejón-Pita, J. R., et al. "Experiments and Lagrangian simulations on the formation of droplets in drop-on-demand mode." *Physical Review E* 83.3 (2011): 036306.

[10] Tan, Hua, An adaptive mesh refinement based flow simulation for free-surfaces in thermal inkjet technology. International Journal of Multiphase Flow. 82, 1-16, 2016.

[11] Furlani, E. P., and M. S. Hanchak. "Nonlinear analysis of the deformation and breakup of viscous microjets using the method of lines." *International Journal for Numerical Methods in Fluids* 65.5 (2011): 563-577.

[12] Hanchak, Michael Stephen. *One dimensional model of thermo-capillary driven liquid jet break-up with drop merging*. Diss. University of Dayton, 2009.

[13] Lee, Yongho. "Analytical solutions of channel and duct flows due to general pressure gradients." *Applied Mathematical Modelling* 43 (2017): 279-286.

[14] Fromm, J. "A numerical study of drop-on-demand ink jets." (1982).

[15] Roy, J., and R. L. Adams. "A one-dimensional numerical model of a drop-on-demand ink jet." *Journal of Applied Mechanics* 53.1 (1986): 193-197.

[16] Schiesser, William E. *The numerical method of lines: integration of partial differential equations*. Elsevier, 2012.

[17] Wijshoff, Herman. "The dynamics of the piezo inkjet printhead operation." *Physics reports* 491.4 (2010): 77-177.
[18] White, Frank M., and Isla Corfield. *Viscous fluid flow*. Vol. 3. New York: McGraw-Hill, 2006
[19] Langlois, William E., and Michel O. Deville. *Slow viscous flow*. Springer Science & Business Media, 2014.
[20] Notz, Patrick K., and Osman A. Basaran. "Dynamics and breakup of a contracting liquid filament." *Journal of Fluid Mechanics* 512 (2004): 223-256.